Systematic study of low-energy incomplete-fusion dynamics in the $^{16}O + ^{148}Nd$ system: Role of target deformation

Pankaj K. Giri,[1] D. Singh,[1,*] Amritraj Mahato,[1] Sneha B. Linda,[1] Harish Kumar,[2] Suhail A. Tali,[2] Siddharth Parasari,[2] Asif Ali,[2] M. Afzal Ansari,[2] Rakesh Dubey,[3] R. Kumar,[3] S. Muralithar,[3] and R. P. Singh[3]

[1]*Department of Physics, Central University of Jharkhand, Ranchi 835 205, India*

[2]*Department of Physics, Aligarh Muslim University, Aligarh 202 002, India*

[3]*NP-Group, Inter-University Accelerator Centre, New Delhi 110 067, India*

(Received 27 January 2019; revised manuscript received 20 June 2019; published 22 August 2019)

A study of low-energy incomplete fusion was done by the measurements of excitation functions of evaporation residues produced in the $^{16}O + ^{148}Nd$ system at energies ≈4–7 MeV/nucleon. The stacked foil activation technique using offline γ-ray spectrometry was employed. Significant enhancements were found in the measured cross sections from the theoretical predictions of PACE-4 for the evaporation residues populated through α-emission channels. This enhancement is attributed to incomplete fusion (ICF) of ^{16}O with ^{148}Nd. The comparison of present work with literature data shows that the ICF probability increases exponentially with existing entrance channel parameters. The dependence of ICF dynamics on target deformation was investigated using deformation parameter (β_2^T), deformation length ($\beta_2^T R^T$) and neutron excess $(N-Z)^T$ of the target. The present analysis indicates that the ICF fraction rises exponentially with β_2^T, $\beta_2^T R^T$, and $(N-Z)^T$. These results show that the ICF fraction follows a systematic exponential pattern rather than a simple linear growth with various entrance channel parameters reported in the literature. However, this study also suggests that the ICF dynamics is strongly influenced by the structure of projectile along with that of the target. Further, the role of deformation parameters on incomplete-fusion dynamics was also investigated through the method of universal fusion function. Analysis of the present data indicates that the experimental fusion functions are suppressed with different factors depending on deformation of the target nuclei. These suppressions are removed by including incomplete-fusion cross sections in the fusion function calculations. The average value of experimental fusion functions deviates from the universal fusion function for deformed targets. However, the average value of the total fusion function for deformed targets shifts towards the average value of the universal fusion function. The present study shows that the effect of target deformation plays an important role in affecting the ICF dynamics, along with various entrance channel parameters for different systems.

DOI: 10.1103/PhysRevC.100.024621

I. INTRODUCTION

Heavy-ion induced reactions at energies above the Coulomb barrier have been a subject of growing interest to nuclear physicists. It has been observed that complete fusion (CF) and incomplete fusion (ICF) are the dominant modes in heavy-ion interaction at energies above the Coulomb barrier [1–4]. The first experimental evidence of ICF was observed by Britt and Quinton [5]. However, major advancement on the study of ICF took place after the study of Inamura *et al.* [6], which provided significant information about ICF dynamics from γ-ray multiplicity measurements. Further, the dependence of localization of the entrance channel angular momentum (ℓ) window on deformation of the target was summarized by Gerschel [7]. Studies of ICF dynamics by the measurement of excitation functions (EFs) of the evaporation residues (ERs) have been done by several investigators [8–10]. Morgenstern *et al.* [11] observed that a more mass-asymmetric system has relatively higher ICF contribution than that of a less mass-asymmetric system at the same relative velocity. Further, systematic studies [12–14] on the dependence of ICF on various entrance channel parameters, namely, entrance channel mass-asymmetry (μ_{EC}^{AS}), α-Q value, $Z_P Z_T$, etc., have also been done. These studies show that a single entrance channel parameter is not able to explain completely the measured yields of the incomplete-fusion dynamics at low energy. Recently, Singh *et al.* [15] revealed that the ICF dynamics also depend on deformation of the target, according to the measurement of spin distributions of ERs using the particle-γ coincidence technique. Various theoretical models have been proposed to explain the characteristics of ICF dynamics. Udagawa and Tamura [16] proposed the breakup fusion (BUF) model to explain the kinetic energy spectra and angular distributions of emitted particles. The sum-rule model was given by Wilczynski *et al.* [17], based on a generalized concept of the critical angular momentum for complete fusion (CF). Other theoretical models, e.g., the promptly emitted particles (PEP) model [18], the hot spot model [19], etc., were also

*Corresponding author: dsinghcuj@gmail.com, dsinghiuac@gmail.com

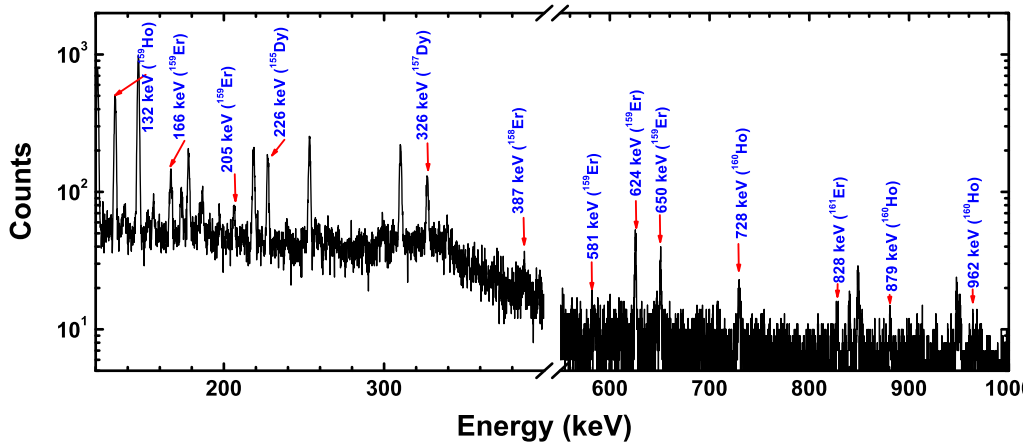

FIG. 1. A typical calibrated γ-ray spectrum of $^{16}\mathrm{O} + {}^{148}\mathrm{Nd}$ system at projectile energy 94.7 ± 0.9 MeV.

proposed to explain various characteristics of ICF. However, none of these models explain satisfactorily the ICF data at low projectile energy. The development of a theoretical model to explain ICF is still an unresolved area of investigation. The universal fusion function (UFF) suggested by Canto *et al.* [20,21] is an important method to observe the role of various entrance channel parameters on ICF dynamics. In this method the measured fusion cross sections are compared with the universal fusion function (UFF) in heavy-ion interaction. This method is based on the one-dimensional barrier penetration model proposed by Wong [22].

In view of these aspects, a systematic study of low-energy incomplete-fusion dynamics in the $^{16}\mathrm{O} + {}^{148}\mathrm{Nd}$ system was carried out to observe the effect of target deformation on ICF dynamics. Measurements of the excitation functions (EFs) of different evaporation residues (ERs), produced through CF and/or ICF in the $^{16}\mathrm{O} + {}^{148}\mathrm{Nd}$ system in the projectile energy range $\approx$4–7 MeV/nucleon, were done. The measured EFs were analyzed in the framework of the statistical model code PACE-4 [23]. Further, an attempt was made to investigate the role of target deformation on ICF dynamics through a new parameter, namely, target deformation length ($\beta_2^T R^T$). In addition, the target structure effect was studied through another new parameter, the neutron excess $(N - Z)^T$ of the target. Moreover, the measured cross sections were also compared with the UFF for the present system along with some other systems available in the literature. To the best of our knowledge, the present results for the above-mentioned system are the first reported. The present paper is organized as follows: experimental methodology is presented in Sec. II, with results and discussion given in Sec. III. A comparison of measured ICF yield with the sum-rule model is discussed in Sec. IV. Systematics of the dependence of ICF on deformation parameters is described in Sec. V. Finally, a summary and conclusions of the present work are given in Sec. VI.

II. EXPERIMENTAL METHODOLOGY

The present experiment was carried out using the 15UD Pelletron accelerator facility at Inter-University Accelerator Centre (IUAC), New Delhi, India. This experiment was performed using the General Purpose Scattering Chamber (GPSC), which has an in-vacuum transfer facility (IVTF) to minimize the time lapse between stop of irradiation and start of counting. The stacked foil activation technique was employed in this experiment. The targets of ^{148}Nd, with enrichment $\approx$98.4%, were prepared by vacuum evaporation technique in the laboratory of target fabrication at IUAC, New Delhi, India. Thickness of the targets used in the stack was in the range $\approx$100–300 μg/cm^2. The target material was deposited on an aluminium (Al) backing of thickness $\approx$1.2–1.7 mg/cm^2. These Al-backing foils were prepared by the rolling technique. The thickness of targets was measured by α-particle transmission (using a ^{241}Am source) as well as the Rutherford backscattering (RBS) method [24]. The purity of the target material was checked using the energy dispersive spectroscopy (EDS) technique. Target foils along with Al backing were pasted on stainless steel holders. These holders have concentric holes of diameter 1 cm. A stack of seven ^{148}Nd targets with Al backings was irradiated by a $^{16}\mathrm{O}^{7+}$ beam of energy $\approx$100 MeV. The stack was irradiated for $\approx$10 hours due to the half-lives of interest of the evaporation residues. The beam current was $\approx$2–3 pnA during the irradiation of targets. Energy loss of the incident beam on successive targets was calculated using software SRIM-2008 [25].

The activities' buildup in the irradiated samples was recorded immediately for each target at different time intervals by using a 100 cm^3 n-type high purity germanium (HPGe) detector coupled to a PC through a computer-aided measurement and control (CAMAC) based data acquisition system. The software CANDLE [26] was used for the recording and offline analysis of the measured data.

The energy and efficiency calibration of the HPGe detector was done using the $^{152}\mathrm{Eu}^g$ standard γ-ray source of known strength. The energy resolution of the detector was found to be $\approx$2.3 keV at the 1408 keV γ ray of the $^{152}\mathrm{Eu}^g$ source. The spectroscopic data of ERs used for yield measurements such as γ-ray energies and their branching ratios, half-lives of ERs, etc., were taken from the Table of Isotopes [27,28].

A list of identified ERs produced via CF and/or ICF dynamics in the $^{16}\mathrm{O} + {}^{148}\mathrm{Nd}$ system along with their decay

TABLE I. List of identified evaporation residues and spectroscopic properties produced in the $^{16}O + ^{148}Nd$ system via complete and/or incomplete fusion.

S. No.	Evaporation residues with channels	Half-life ($T_{1/2}$)	Energy of γ ray (keV)	Branching ratio (θ%)
1	$^{161}Er(3n)$	3.21 h	827	64.00
			593	3.70
			315	2.50
2	$^{159}Er(5n)$	36.00 min	625	33.00
			650	23.40
			206	9.70
			167	5.00
			581	4.00
3	$^{158}Er(6n)$	2.29 h	387	9.00
			248	3.40
4	$^{161}Ho(p2n)$	2.48 h	103	3.90
5	$^{160}Ho(p3n)$	25.60 min (g)	728	14.60
			879	9.56
		5.02 h (m)	962	25.60
			645	24.70
6	$^{159}Ho(p4n)$	33.00 min	132	23.60
7	$^{157}Dy(\alpha 3n)$	8.10 h	326	92.00
8	$^{155}Dy(\alpha 5n)$	10.00 h	226	68.40
			184	3.37
9	$^{155}Tb(\alpha p4n)$	5.32 d	180	7.45
			262	5.30
			163	4.44

(m)=metastable state, (g)=ground state, min=minutes, (h)=hours, d=days

characteristics is given in Table I. A typical calibrated γ-ray spectrum of the $^{16}O + ^{148}Nd$ system at projectile energy 94.7 ± 0.9 MeV is shown in Fig. 1. Different γ-ray peaks were assigned to evaporation residues produced through CF and/or ICF channels. The ERs were identified by observing their characteristic γ rays and following the decay curve analysis. The decay curves of ERs ^{159}Er ($T_{1/2} = 36$ min), ^{160m}Ho ($T_{1/2} = 5.02$ h) and ^{155}Tb ($T_{1/2} = 5.32$ d) recorded at beam energy 99.90 MeV are shown in Fig. 2. The experimental reaction cross sections $\sigma_{ER}(E)$ were calculated at each projectile energy by using the following standard prescription as given in Ref. [29]:

$$\sigma_{ER}(E) = \frac{A\lambda \exp(\lambda t_2)}{N_0 \varphi \epsilon_G \theta K[1 - \exp(-\lambda t_1)][1 - \exp(-\lambda t_3)]} \quad (2.1)$$

where, A is the photopeak area of the characteristic γ ray, λ is the decay constant of the ER, N_0 is the number of target nuclei per unit area, φ is the incident ion beam flux, ϵ_G is the geometry dependent efficiency, θ is the branching ratio of the characteristic γ ray, t_1 is the irradiation time, t_2 is the time elapsed between stop of irradiation and start of the counting of the individual target along with backing, and t_3 is the counting time. $K = \exp(-\mu d)$ is the correction for self-absorption of the γ ray with the absorption coefficient μ for the target of thickness d.

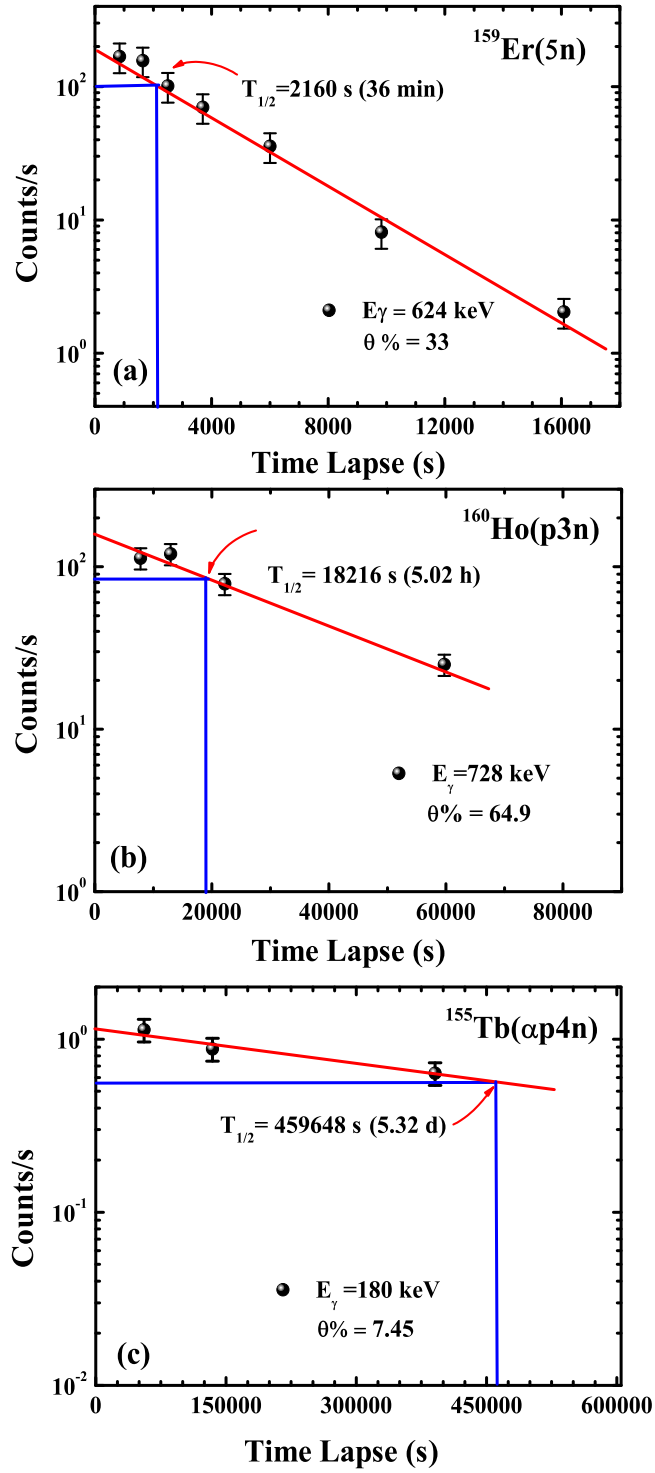

FIG. 2. The decay curves of ERs ^{159}Er ($T_{1/2} = 36$ min), ^{160}Ho ($T_{1/2} = 5.02$ h) and ^{155}Tb ($T_{1/2} = 5.32$ d) detected at beam energy 99.90 MeV.

TABLE II. The measured cross sections for the ERs ^{161}Er($3n$), ^{159}Er($5n$), and ^{158}Er($6n$) along with their estimated errors obtained in the ^{16}O + ^{148}Nd system at different projectile energies.

$E_{\rm Lab}$ (MeV)	$\sigma^{\rm Expt}_{\rm Indp}$ (^{161}Er) (mb)	$\sigma^{\rm Expt}_{\rm Indp}$ (^{159}Er) (mb)	$\sigma^{\rm Expt}_{\rm Indp}$ (^{158}Er) (mb)
67.20 ± 0.26	31.30 ± 0.89		
72.40 ± 0.10	30.29 ± 0.97		
77.40 ± 0.18	15.87 ± 0.52	137.28 ± 19.34	
84.10 ± 0.11	5.90 ± 0.75	380.42 ± 11.35	13.90 ± 3.06
89.10 ± 0.17		520.66 ± 12.70	38.08 ± 4.20
94.70 ± 0.17		511.66 ± 12.07	230.87 ± 7.77
99.90 ± 0.09		353.03 ± 9.48	535.88 ± 13.91

TABLE IV. The measured cross sections for the ERs ^{157}Dy($\alpha 3n$), ^{155}Dy($\alpha 5n$), and ^{155}Tb($\alpha p4n$) along with their estimated errors obtained in the ^{16}O + ^{148}Nd system at different projectile energies.

$E_{\rm Lab}$ (MeV)	$\sigma^{\rm Expt}_{\rm Indp}$ (^{157}Dy) (mb)	$\sigma^{\rm Expt}_{\rm Indp}$ (^{155}Dy) (mb)	$\sigma^{\rm Expt}_{\rm Indp}$ (^{155}Tb) (mb)
67.20 ± 0.26	3.14 ± 0.19		
72.40 ± 0.10	14.21 ± 1.52		
77.40 ± 0.18	39.61 ± 2.95		
84.10 ± 0.11	40.67 ± 1.68	47.13 ± 4.23	7.80 ± 1.17
89.10 ± 0.17	35.69 ± 1.04	52.33 ± 3.83	13.79 ± 2.08
94.70 ± 0.17	33.75 ± 1.04	51.78 ± 3.82	17.22 ± 2.72
99.90 ± 0.09	38.29 ± 1.14	74.01 ± 3.31	10.52 ± 1.50

Several factors are responsible for the uncertainties in the measured cross sections. The main factors are the following: (i) The uncertainty due to the nonuniformity of the target and thickness measurement was estimated to be less than 3%. (ii) The uncertainty in the efficiency calibration of the HPGe detector was estimated to be less than 5%. (iii) The error arising from the fluctuations in beam current is estimated to be less than 6%. (iv) To minimize the error, the counting was done for dead time below 10%. (v) Uncertainty due to the straggling effect of the projectile passing through the stack was estimated to be less than 2%. The overall uncertainties from various factors including statistical errors in the photopeak area are estimated to be <15%. The measured cross sections for the production of various ERs obtained for the system ^{16}O + ^{148}Nd at different beam energies along with the estimated errors are tabulated in Tables II–IV.

III. RESULTS AND DISCUSSION

Excitation functions of ERs ^{161}Er($3n$), ^{159}Er($5n$), ^{158}Er($6n$), ^{161}Ho($p2n$), ^{160}Ho($p3n$), ^{159}Ho($p4n$), ^{157}Dy($\alpha 3n$), ^{155}Dy($\alpha 5n$), and ^{155}Tb($\alpha p4n$) produced through CF and ICF dynamics in the ^{16}O + ^{148}Nd system were measured in the projectile energy range ≈4–7 MeV/nucleon. The analysis of the present data was carried out using the statistical model code PACE-4, which follows the Monte Carlo simulation procedure for deexcitation of a compound nucleus (CN). This code is based on the Hauser-Feshbach formalism of CN decay [30]. The angular momentum projections are calculated at each stage of deexcitation of CN to determine the angular distribution of emitted particles. The CF cross sections are calculated using the Bass formula [31]. The transmission coefficients for light particles are calculated using the optical model potentials of Becchetti and Greenlees [32]. The γ-ray strength functions required for $E1$, $E2$, and $M1$ transitions are taken from the tables of Endt [33]. Masses of the particles are taken from the atomic mass table [34]. In this code, the level density parameter a ($=A/K$) MeV^{-1} is an important parameter, where A is the mass number of the CN and K is the level density parameter constant. Most of the input parameters were taken as default in this code.

A. Excitation functions of CF (*xn* and *pxn* emitting) channels

The ERs ^{161}Er($3n$), ^{159}Er($5n$), ^{158}Er($6n$), ^{161}Ho($p2n$), ^{160}Ho($p3n$), and ^{159}Ho($p4n$) are populated through the emission of *xn* and *pxn* channels in the system ^{16}O + ^{148}Nd. No precursor contributions for these ERs were observed. The measured EFs of these ERs were plotted along with theoretical predictions of PACE-4 code and are shown in Figs. 3 and 4. To find out the suitable value of level density a ($=A/K$) MeV^{-1} for comparison with measured data, different values of parameter K were chosen. The value of $K > 10$ may give rise to anomalous effects in the particle multiplicity and CN temperature [35]. In this comparison, the value of K found to be suitable for best fit with the measured data is $K = 10$ for the *xn* and *pxn* emission channels. It can be seen from Fig. 3 that the measured cross sections of ERs ^{161}Er, ^{159}Er, and ^{158}Er are satisfactorily reproduced with theoretical predictions of PACE-4 along with available data from Broda [36] for

TABLE III. The measured cross sections for the ERs ^{161}Ho($p2n$), ^{160}Ho($p3n$), and ^{159}Ho($p4n$) along with their estimated errors obtained in the ^{16}O + ^{148}Nd system at different projectile energies.

$E_{\rm Lab}$ (MeV)	$\sigma^{\rm Expt}_{\rm Cumt}$(^{161}Ho) (mb)	$\sigma^{\rm Expt}_{\rm Cumt}$(^{160m}Ho) (mb)	$\sigma^{\rm Expt}_{\rm Cumt}$(^{160g}Ho) (mb)	$\sigma^{\rm Expt}_{\rm Cumt}$(^{159}Ho) (mb)
67.20 ± 0.26	35.63 ± 4.08	68.40 ± 7.67	100.59 ± 13.59	
72.40 ± 0.10	24.27 ± 2.12	43.87 ± 3.06	256.64 ± 33.36	50.61 ± 7.79
77.40 ± 0.18	9.62 ± 0.90	57.31 ± 7.53	283.62 ± 36.87	75.65 ± 11.06
84.10 ± 0.11		59.78 ± 8.89	154.84 ± 20.13	510.06 ± 38.11
89.10 ± 0.17		36.62 ± 6.90	113.81 ± 14.79	657.18 ± 47.46
94.70 ± 0.17		10.97 ± 1.98	42.4 ± 5.46	547.05 ± 39.33
99.90 ± 0.09			12.3 ± 1.56	450.06 ± 30.58

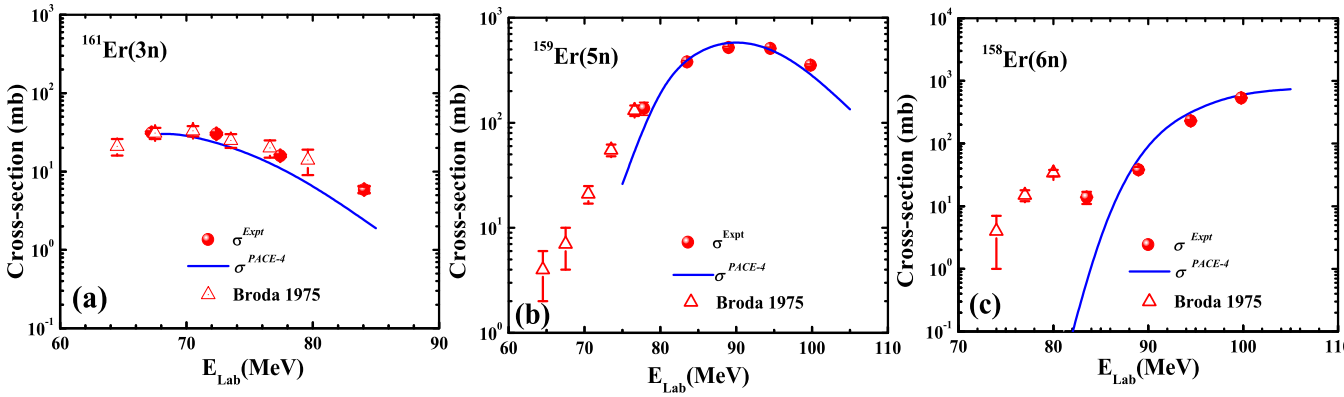

FIG. 3. Measured excitation functions of ERs ^{161,159,158}Er populated through the emission of $3n$, $5n$, and $6n$ channels in the $^{16}O + ^{148}Nd$ system. Solid spheres, hollow triangles, and solid curves represent the measured cross sections, data from Broda [36], and predictions of PACE-4 code respectively.

xn channels at the lower energy side. The agreement of present results with earlier measurements also validates the present measurements along with PACE-4 code. These ERs are populated through only CF of ^{16}O with target ^{148}Nd. On the other hand, the ERs ^{161}Ho($p2n$), ^{160}Ho($p3n$), and ^{159}Ho($p4n$) are populated through the emission of protons and neutrons from the compound nucleus ^{164}Er*. These ERs may also be populated through β^+/EC (electron capture) decay of their higher charge precursor isobars ^{161}Er($3n$), ^{160}Er($4n$), and ^{159}Er($5n$). The measured cross sections of these ERs will be the cumulative cross sections. These ERs have half-lives comparable with their higher charge precursor isobars. In this context, extraction of independent cross sections from cumulative cross sections is very difficult for these ERs. An effort was made to compare the measured cumulative cross sections with theoretical cumulative cross sections of PACE-4 code in this case, as shown in Fig. 4. The theoretical cumulative cross sections

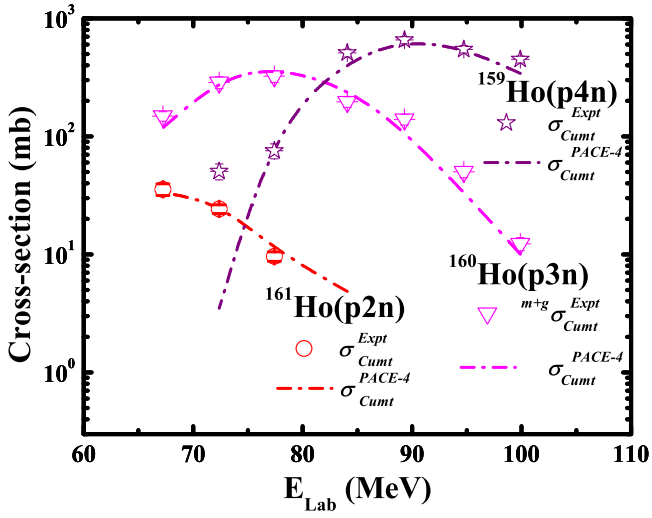

FIG. 4. Measured excitation functions of evaporation residues ^{161,160,159}Ho populated through the emission of $p2n$, $p3n$, and $p4n$ channels in the $^{16}O + ^{148}Nd$ system. Hollow symbols represent the measured cumulative cross sections and dash-dotted curves show theoretical cumulative cross sections estimated by PACE-4 code.

are the sum of cross sections of ERs and their higher charge precursor isobars, calculated using code PACE-4. From this figure, it is clear that the measured cumulative cross sections are in good agreement with theoretical cumulative cross sections of PACE-4 code. These results clearly indicate that these ERs, ^{161}Ho, ^{160}Ho, and ^{159}Ho, are also populated through CF. The value of level density parameter $a = A/10$ MeV^{-1} was used for further analysis of data for αxn and αpxn emitting channels in the present work by taking the same set of parameters.

B. Excitation functions of ICF (αxn and αpxn emitting) channels

The measured cross sections of ERs ^{157}Dy($\alpha 3n$), ^{155}Dy($\alpha 5n$), and ^{155}Tb($\alpha p4n$) produced through α-emission channels along with theoretical predictions of PACE-4 code are displayed in Fig. 5. No precursor contribution for the ERs ^{157}Dy($\alpha 3n$) and ^{155}Dy($\alpha 5n$) were observed during analysis of data. Thus, the measured cross sections of these ERs will be independent. In Figs. 5(a) and 5(b), the measured cross sections are found to be significantly enhanced compared to the theoretical cross sections of PACE-4. The PACE-4 code does not produce the ICF contributions. Hence, the enhancement in measured cross sections over theoretical cross sections is attributed to the incomplete fusion of the projectile ^{16}O (i.e., breakup of projectile ^{16}O into $^{12}C + \alpha$) with the ^{148}Nd target. The composite system formed during the ICF process will decay through the subsequent emission of neutrons and protons. These results indicate that ERs ^{157}Dy and ^{155}Dy may be populated not only via the CF of ^{16}O but also through ICF. The ERs ^{157}Dy and ^{155}Dy may be populated via two different reaction routes represented as follows:

(i) CF of ^{16}O with ^{148}Nd:

$$^{16}O + ^{148}Nd \rightarrow [^{164}Er]^* \rightarrow ^{157,155}Dy + \alpha xn\ (x = 3, 5).$$

(ii) ICF of ^{16}O (i.e., fusion of the fragment ^{12}C):

$$^{16}O(^{12}C + \alpha) + ^{148}Nd \rightarrow ^{12}C + ^{148}Nd + \alpha\ \text{(spectator)}$$
$$\rightarrow [^{160}Dy]^* + \alpha\ \text{(spectator)}$$
$$^{160}Dy^* \rightarrow ^{157,155}Dy + xn\ (x = 3, 5).$$

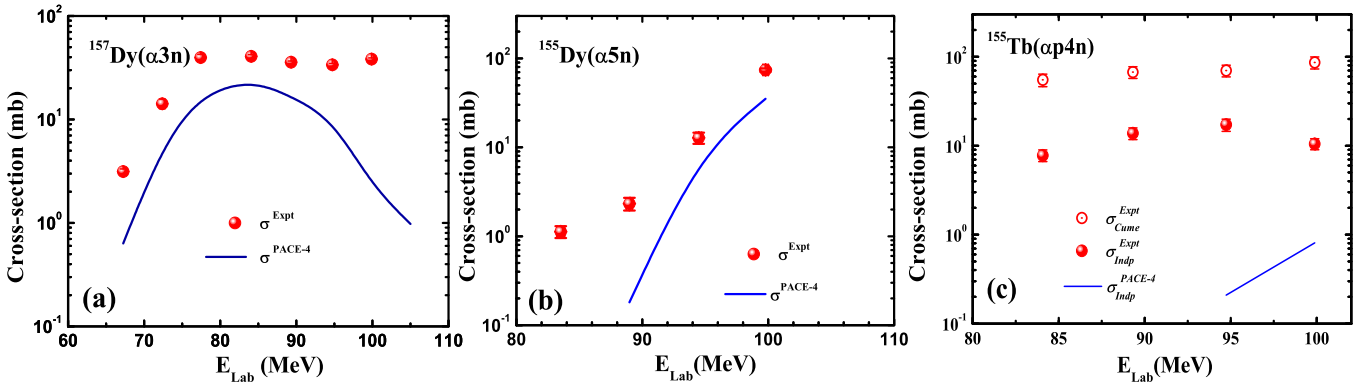

FIG. 5. Excitation functions of evaporation residues (a),(b) ^{157,155}Dy and (c) ^{155}Tb populated through $\alpha 3n$, $\alpha 5n$, and $\alpha p4n$ reaction channels. Solid spheres are for the independent cross section data and hollow spheres are for the cumulative cross section. Solid curves are the PACE-4 predicted cross sections.

The ER ^{155}Tb($\alpha p4n$) may also be populated through β^+/EC decay of their higher charge precursor isobar ^{155}Dy($\alpha 5n$). The measured cross sections of this ER will be the cumulative cross sections. To separate out the precursor contribution from the cumulative cross-section, an attempt was made using the prescription suggested by Cavinato *et al.* [37]. In this case the independent cross sections of ER ^{155}Tb($\alpha p4n$) were extracted from their cumulative cross section using the following expression:

$$\sigma_{\text{Indp}}^{^{155}\text{Tb}} = \sigma_{\text{Cumt}}^{^{155}\text{Tb}} - 1.02\sigma_{\text{Indp}}^{^{155}\text{Dy}} \tag{3.1}$$

Significant enhancement is observed in the measured independent cross sections of ER ^{155}Tb($\alpha p4n$) compared to the theoretical predictions of PACE-4, as shown in Fig. 5(c). This indicates that the ER ^{155}Tb may also populate through ICF along with CF of projectile ^{16}O with target ^{148}Nd. This ER may be populated via three different reaction routes as follows:

(i) CF of ^{16}O with ^{148}Nd:

$$^{16}\text{O} + {}^{148}\text{Nd} \rightarrow [{}^{164}\text{Er}]^* \rightarrow {}^{155}\text{Tb} + \alpha pxn \ (x = 4).$$

(ii) ICF of ^{16}O (i.e., fusion of the fragment ^{12}C):

$$^{16}\text{O}(^{12}\text{C} + \alpha) + {}^{148}\text{Nd} \rightarrow {}^{12}\text{C} + {}^{148}\text{Nd} + \alpha \text{ (spectator)}$$
$$\rightarrow [{}^{160}\text{Dy}]^* + \alpha \text{ (spectator)}$$
$$^{160}\text{Dy}^* \rightarrow {}^{155}\text{Tb} + p4n.$$

(iii) Through EC/β^+ decay of the produced higher charge precursor isobar:

$$^{155}\text{Dy} \xrightarrow{\beta^+/EC} {}^{155}\text{Tb}.$$

IV. A COMPARISON OF MEASURED ICF YIELD WITH THE SUM-RULE MODEL

The sum-rule model, explained by Wilczynski *et al.* [17], is a widely used theoretical model of ICF. The Sumrule model is based on the generalized concept of critical angular momentum (ℓ_{crit}) for CF of the projectile with the target. This model successfully predicted the ICF cross sections at projectile energy above 10 MeV/nucleon and the localization of the various reactions in ℓ windows. In the present work, the cross sections of ERs populated through CF and/or ICF channels in the interaction of projectile ^{16}O with target ^{148}Nd were also calculated using the sum-rule model. This model contains several important parameters; namely, the temperature of the contact zone between the interacting partners (T), the diffuseness parameter (Δ) of the transmission probability distribution (T_l), and the Coulomb interaction radius (R_c). These parameters were taken as 3.5 MeV, 1.7$\hbar$ and 11.25 fm respectively, as suggested by Wilczynski *et al.* [17]. The total transfer yields in ICF (α-emission) channels in the projectile energy range ≈4–7 MeV/nucleon were estimated from the measured data. These measured total transfer yields were compared with the sum-rule model predictions for the present system and are displayed in Fig. 6. The graph shows that the measured total transfer yields of ICF (α-emission) channels are much higher than those of cross sections of sum-rule model for the entire projectile energy range. These

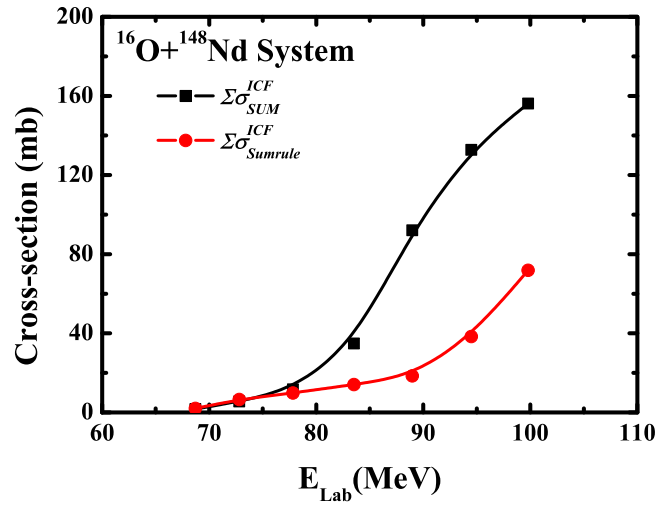

FIG. 6. A comparison of total transfer yield of measured and sum-rule model predictions for ICF (α-emitting) channels in the system ^{16}O + ^{148}Nd at energies ≈4–7 MeV/nucleon.

results indicate that the sum-rule model does not successfully predict the ICF cross sections at projectile energies ≈4–7 MeV/nucleon. It means that the sum-rule model is not valid for low projectile energy.

V. SYSTEMATICS OF THE DEPENDENCE OF ICF ON DEFORMATION PARAMETERS

An attempt was made to separate out the ICF contribution from the measured data of the $^{16}O + ^{148}Nd$ system at energies ≈4–7 MeV/nucleon. As already mentioned, the enhancement in the measured production cross sections over the PACE-4 predictions in some evaporation residues may be attributed to the incomplete-fusion process. The ICF contribution (σ^{ICF}) for individual channels was estimated by subtracting the theoretically calculated complete-fusion cross sections by PACE-4 from the measured cross sections at each projectile energy. The total incomplete-fusion cross section (σ^{ICF}_{Sum}) was obtained by adding the incomplete-fusion cross sections of different measured evaporation residues at each projectile energy. The total complete-fusion cross section (σ^{CF}_{Sum}) was calculated using the measured data of CF channels and predictions of PACE-4 code for unmeasured ERs at each projectile energy. Some of the ERs are not detected due to their very short or long half-lives and low intense γ rays. It is well known that the measured cross sections of CF channels are satisfactorily reproduced by PACE-4 code. Hence, the predictions of PACE-4 code for unmeasured ERs of CF channels were used in the calculation of total complete-fusion cross section (σ^{CF}_{Sum}). However, for the ERs formed through the ICF process, no such modification could be applied due to the unavailability of theoretical code that may predict the ICF contribution at low projectile energy. Therefore, the estimated value of total ICF contribution (σ^{ICF}_{Sum}) should be treated as a lower limit of ICF for the present system $^{16}O + ^{148}Nd$. The comparisons of measured data also rely on theoretical estimations due to the experimental limitations. The total fusion cross section (σ^{CF+ICF}_{TF}) was obtained by adding σ^{CF}_{Sum} and σ^{ICF}_{Sum}. The ICF fraction $F_{ICF}(\%)$ is defined as the $F_{ICF}(\%) = (\sigma^{ICF}_{Sum}/\sigma^{CF+ICF}_{TF}) \times 100$. The ICF fraction $F_{ICF}(\%)$ is a measure of strength of ICF relative to total fusion (CF and ICF). The measured incomplete-fusion fraction $F_{ICF}(\%)$ for the present system $^{16}O + ^{148}Nd$ along with some earlier measurements [38–50] was deduced at a constant value of normalization factor $(\ell_{max} - \ell_{crit})/\ell_{max} = 0.096$. The factor $(\ell_{max} - \ell_{crit})/\ell_{max}$ was introduced in Ref. [43] for normalization of data to disentangle the entrance channel effects on ICF dynamics, where ℓ_{max} and ℓ_{crit} are the maximum and critical angular momenta of the systems. Their values were calculated using prescription [17]. In this parameter the angular momentum limit of CF and ICF channels is considered, and therefore this factor is more suitable than other normalization factors used earlier for comparison of experimental data for different systems.

A. Incomplete-fusion fraction with mass asymmetry, Coulomb factor, and α-*Q* value

A critical review was done to understand the dependence of ICF dynamics on entrance channel parameters, e.g., mass asymmetry (μ^{AS}_{EC}) between interacting partners, Coulomb factor ($Z_P Z_T$), and the α-Q value of the projectile. Morgenstern *et al.* [11] observed that the ICF fraction increases linearly

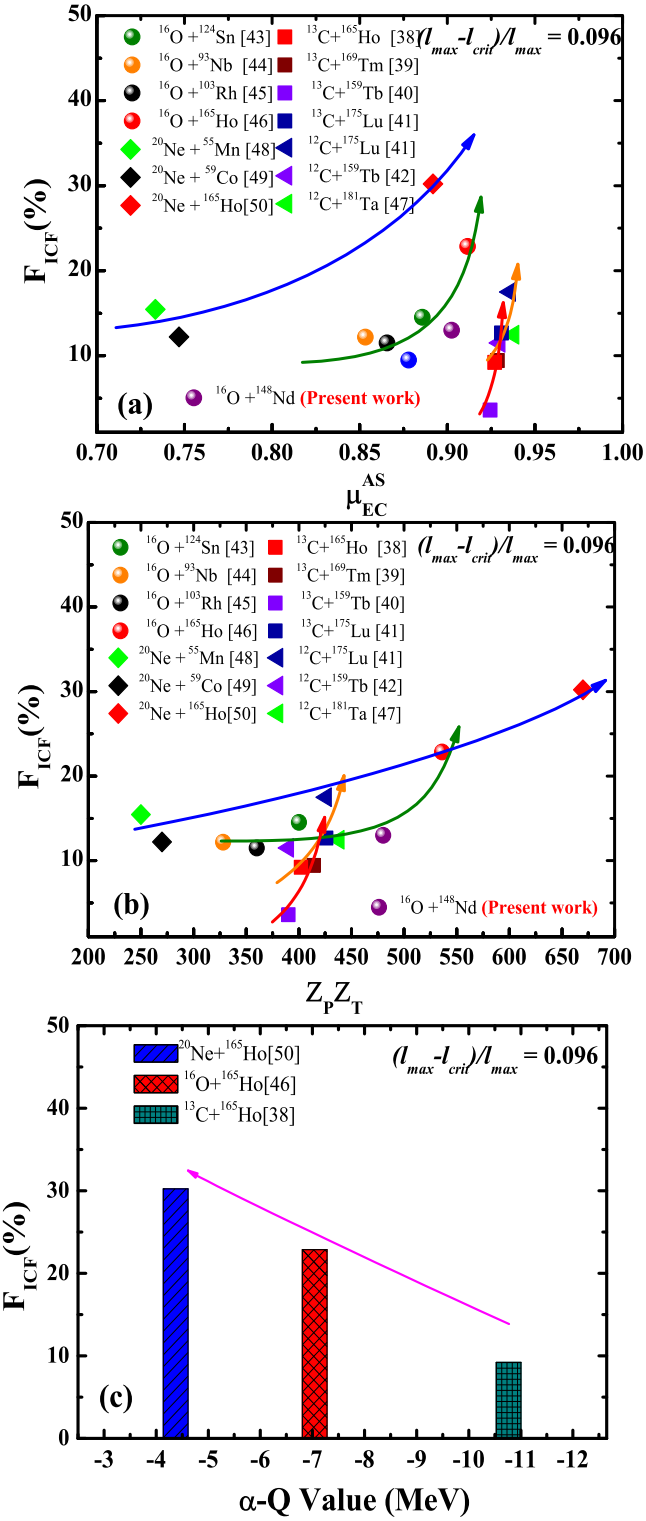

FIG. 7. The incomplete-fusion fraction $F_{ICF}(\%)$ as a function of entrance channel mass asymmetry, Coulomb factor and α-Q value for the $^{16}O + ^{148}Nd$ system with some other systems from literature [38–50] at a constant value $(\ell_{max} - \ell_{crit})/\ell_{max} = 0.096$.

with entrance channel mass asymmetry $[\mu_{EC}^{AS} = A^T/(A^T + A^P)]$. The measured ICF fraction $F_{\rm ICF}(\%)$ for the present system ^{16}O + ^{148}Nd and some earlier measurements [38–50] was plotted as a function of entrance channel mass asymmetry at a constant value $(\ell_{\rm max} - \ell_{\rm crit})/\ell_{\rm max} = 0.096$ and is displayed in Fig. 7(a). This figure shows that the ICF fraction rises exponentially with mass asymmetry, independently for each projectile. These present results clearly show that the entrance channel mass asymmetry and structure of projectile affect the ICF dynamics. In addition, the role of Coulomb factor (Z_PZ_T) on ICF was also studied in the present work. The ICF fraction as a function of Coulomb factor (Z_PZ_T) for the present system and some literature data [38–50] at $(\ell_{\rm max} - \ell_{\rm crit})/\ell_{\rm max} = 0.096$ were plotted and are displayed in Fig. 7(b). It can be seen from this figure that $F_{\rm ICF}(\%)$ shows exponential growth with the Coulomb factor (Z_PZ_T), separately for different projectiles. From this figure, it can be noticed that the systems with same Z_PZ_T have different values of $F_{\rm ICF}(\%)$ fraction in the studied energy region. This Coulomb factor systematics also indicates the projectile structure effect. Further, these results were also confirmed by the systematics of the α-Q value of the projectile. The ICF fractions of systems ^{20}Ne + ^{165}Ho [50], ^{16}O + ^{165}Ho [46], and ^{13}C + ^{165}Ho [38] were plotted as a function of α-Q value of the projectile and are shown in Fig. 7(c). These systems have same target, ^{165}Ho, but different projectiles, ^{20}Ne (α-$Q = -4.73$ MeV), ^{16}O (α-$Q = -7.16$ MeV), and ^{13}C (α-$Q = -10.65$ MeV). It can be seen from this figure that systems with larger α-Q value of the projectile have larger ICF fractions. This present review suggests that ICF dynamics is affected by various entrance channel parameters simultaneously. Recently, similar types of measurements of excitation functions for the ^{12}C + ^{165}Ho system were done at low projectile energy [51]. A systematic study of breakup fusion and its interplay with various entrance channel parameters, i.e., mass asymmetry (μ_{EC}^{AS}) of the system, Coulomb factor (Z_PZ_T), and α-Q value of projectile was done. These measurements indicate that the ICF dynamics depends not on any single entrance channel parameter but is affected by several parameters. Moreover, that study shows a linear rise pattern of ICF fraction with the above mentioned parameters. On the other hand, the present work suggests an exponential growth of ICF fraction with these entrance channel parameters. Furthermore, the present study is mainly focused on the role of target deformation and its structure on ICF dynamics. The correlation of ICF fraction with the deformation or structure of target was studied using three different parameters: deformation of the target (β_2^T), target deformation length ($\beta_2^T R^T$), and neutron excess $(N - Z)^T$ of the target.

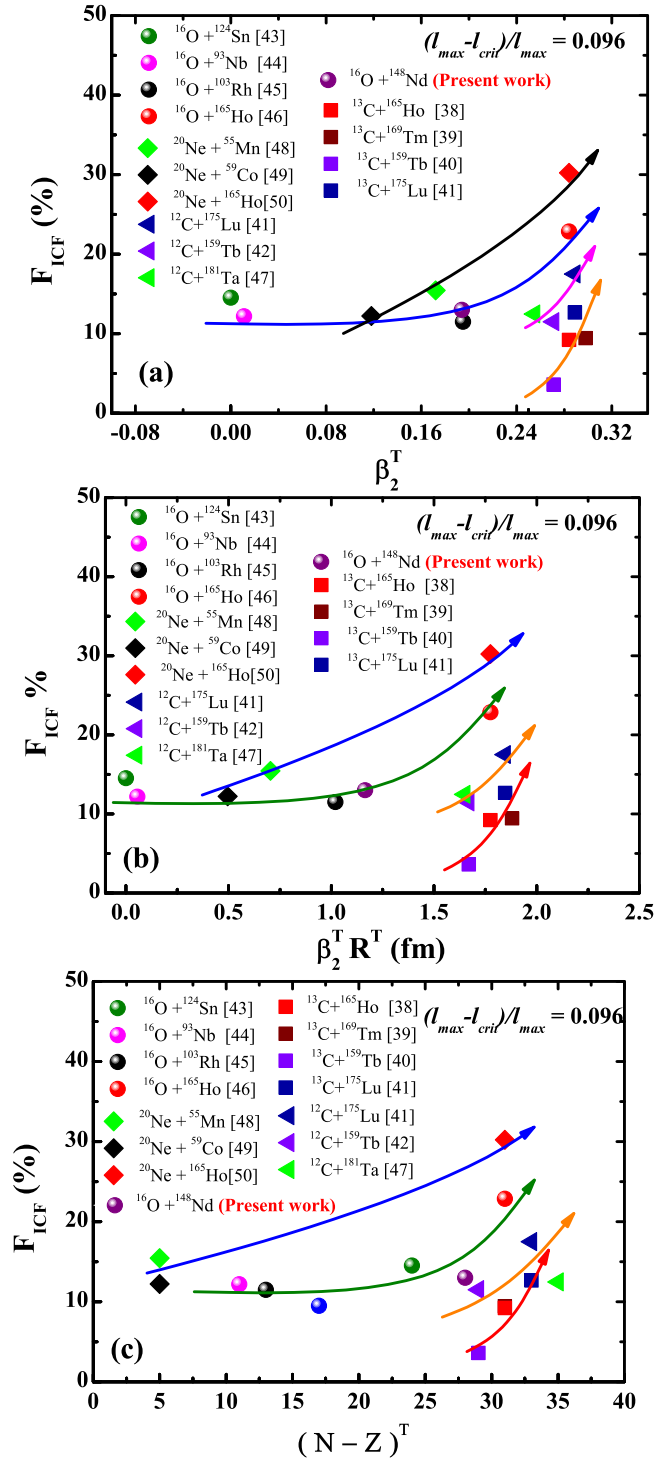

FIG. 8. The incomplete-fusion fraction $F_{\rm ICF}(\%)$ as function of deformation of target (β_2^T), deformation length ($\beta_2^T R^T$), and neutron excess $(N - Z)^T$ of target for the ^{16}O + ^{148}Nd system with some other systems from literature [38–50] at a constant value $(\ell_{\rm max} - \ell_{\rm crit})/\ell_{\rm max} = 0.096$.

B. Effect of target deformation on ICF dynamics

The effect of target deformation on ICF dynamics at low projectile energy is given in this subsection. The shape of a nucleus can be described by the deformation parameter (β_2^T), which is related to the quadrupole moment (Q_0) of the nucleus. More details of the formulation of deformation parameter (β_2^T) are given in Ref. [52]. Recently, it was observed that the ICF dynamics is also affected by deformation of the target, but no definite conclusion regarding this is available in the literature. To get a definite conclusion, a new parameter, target deformation length ($\beta_2^T R^T$), was introduced. The target deformation length ($\beta_2^T R^T$) is the multiplication of

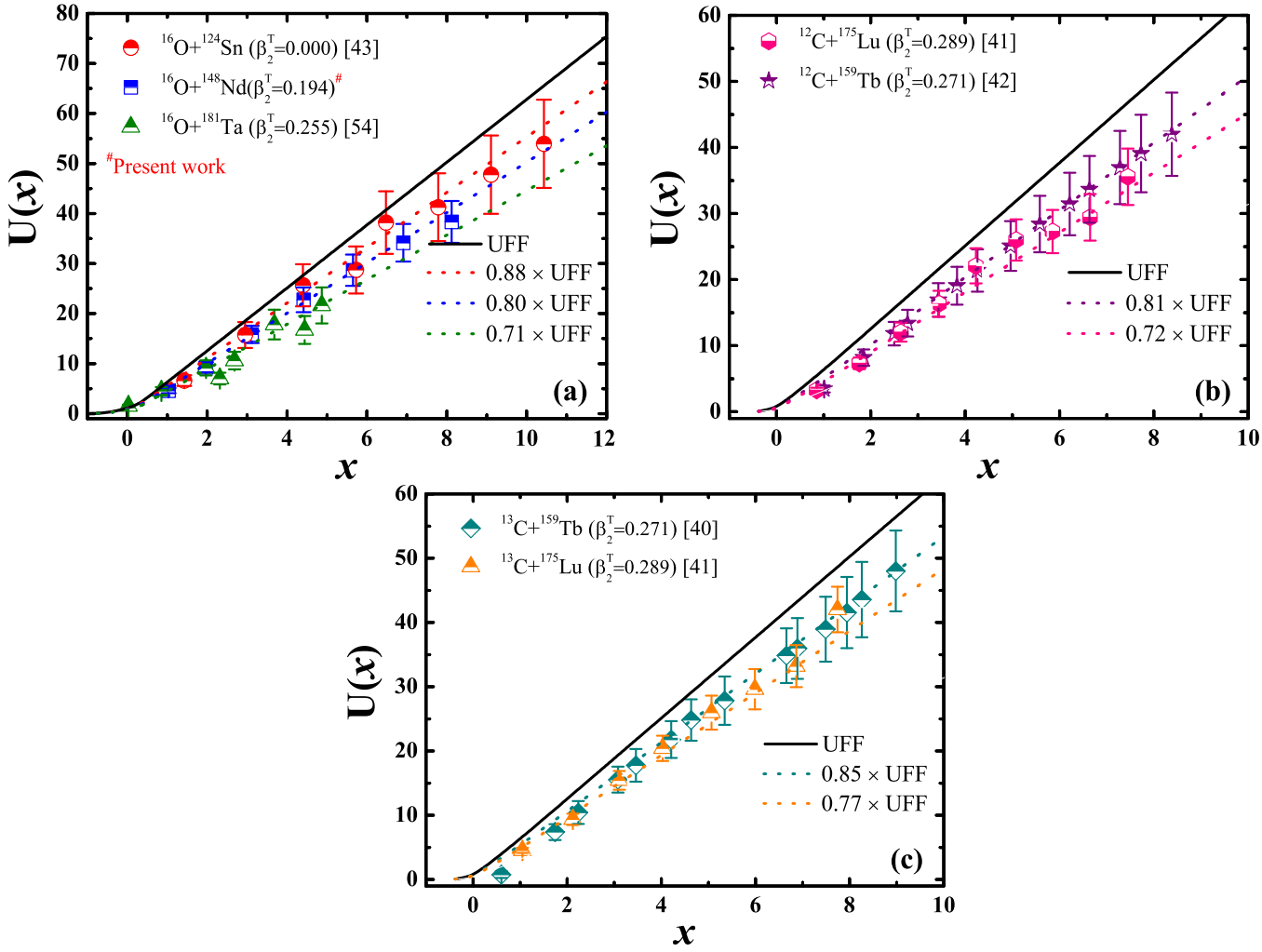

FIG. 9. The experimental fusion functions (EFFs) along with the universal fusion function (UFF) for the $^{16}O + ^{148}Nd$ system with some other systems from literature [40–43,54]. The solid line represents the UFF and dash-dotted lines represent best fits to EFFs for different systems.

target deformation parameter (β_2^T) with mean radius of target (R^T). This parameter provides information about effect of orientation and shape of a nucleus. The β_2^T values of different targets were taken from Ref. [52], while the values of R^T were calculated using the formulation in Ref. [53]. The deduced values of $F_{\rm ICF}(\%)$ for the present system along with other systems [38–50] were plotted as a function of deformation parameter (β_2^T) and target deformation length ($\beta_2^T R^T$), as shown in Figs. 8(a) and 8(b). From these plots, it can be clearly seen that the ICF fraction increases exponentially with both β_2^T and $\beta_2^T R^T$. The results for deformation length are the same as that for β_2^T. This is because the deformation length is also related to the structure of the target. The interaction radius of a system depends on the shape and orientation of interacting nuclei (oblate or prolate). Thus, the total and ICF cross sections are also dependent on the shape and orientation of the nuclei. Target deformation length is also able to probe the effect of shape and orientation of the nuclei. Further, to confirm these results, another new parameter, neutron excess $(N-Z)^T$ of the target, was considered. The $N-Z$ value of the target is also related to the structure of the target and hence it should show the same characteristics as β_2^T and $\beta_2^T R^T$. The ICF fraction for the present system and literature data [38–50] were plotted as a function of $(N-Z)^T$ and are shown in Fig. 8(c). As can be seen clearly in this figure, the ICF fraction rises exponentially also with $(N-Z)^T$, independently for different projectiles. Thus, the effect of structure of the target is shown by three different parameters, e.g., β_2^T, $\beta_2^T R^T$, and $(N-Z)^T$. These present results highlight the role of target structure in ICF dynamics. The critical review of the existing entrance channel effects along with some new parameters indicate that the ICF dynamics is strongly affected by the structure of both projectile as well as target. Earlier studies available in the literature [12–14,38] observed a simple linear pattern of ICF fraction with various entrance channel parameters. However, the present results clearly show that the ICF fraction rises exponentially with entrance channel parameters in contrast to a simple linear growth.

C. Effect of target deformation on ICF dynamics by the universal fusion function (UFF)

The effect of various entrance channel parameters on ICF dynamics for systems involving tightly bound projectiles was also studied using the universal fusion function (UFF). The UFF is a new reduction procedure, suggested by Canto *et al.* [20,21], which completely eliminates the geometrical and static effects of the potential acting between the interacting partners. In this reduction procedure, the fusion cross sections and the incident energy are reduced to a dimensionless equation called the fusion function $U(x)$ and dimensionless variable x as $U(x) = [(2E_{CM})/\hbar\omega R_B^2]\sigma_{\rm Fus}$ and $x = (E_{CM} - E_{CB})/\hbar\omega$, where $\hbar\omega$, R_B, E_{CB}, and E_{CM} are the barrier curvature, barrier radius, Coulomb barrier and the projectile energy in the center-of-mass frame, respectively.

The experimental fusion functions (EFFs) for the present ^{16}O + ^{148}Nd system along with other systems ^{13}C + ^{159}Tb [40], ^{13}C + ^{175}Lu [41], ^{12}C + ^{175}Lu [41], ^{12}C + ^{159}Tb [42], ^{16}O + ^{124}Sn [43], and ^{16}O + ^{181}Ta [54] were plotted as a function of x and are displayed in Fig. 9. The EFFs were determined using total complete-fusion cross sections ($\sigma_{\rm Sum}^{\rm CF}$) for the above mentioned systems. The solid lines in these figures represent the UFF, which was calculated using the prescription in Refs. [20,21]. The UFF is a simple function of dimensionless variable x and is independent of the entrance channel. The couplings of inelastic excitations and transfer channels are not so effective at energies above the Coulomb barrier of the system. Therefore, any deviation in the EFFs from the UFF is attributed to the breakup of the projectile. It can be seen clearly from Figs. 9(a)–9(c), that the EFFs for all the systems are well suppressed. As can be noticed from these figures, the EFFs for the systems having same projectiles (^{16}O, ^{13,12}C), but different values of deformation parameters for targets are suppressed by different factors. The suppression factor for the system ^{16}O + ^{124}Sn ($\beta_2^T = 0.000$) comes out to be 0.88, while for the systems ^{16}O + ^{148}Nd ($\beta_2^T = 0.194$) and ^{16}O + ^{181}Ta ($\beta_2^T = 0.255$) the suppression factors are 0.80 and 0.71 respectively. This means that the contribution of ICF increases with the deformation of the target. However, $F_{\rm ICF}(\%)$ for the system ^{16}O + ^{181}Ta is slightly away from the linear increasing trend. This may be because cross sections of some ERs could not be measured due to limitations of the stacked foil activation technique. Hence, the suppression factor for this system is also very small, i.e., 0.71, which would be expected to go up if all possible α-emitting channels could be measured. On the other hand, the suppression factors for the system ^{12}C + ^{159}Tb ($\beta_2^T = 0.271$) and ^{12}C + ^{175}Lu ($\beta_2^T = 0.289$) are found to be 0.81 and 0.72 respectively and displayed in Fig. 9(b). As can be seen in Fig. 9(c), the suppression factors for the systems ^{13}C + ^{159}Tb ($\beta_2^T = 0.271$) and ^{13}C + ^{175}Lu ($\beta_2^T = 0.289$) are 0.85 and 0.75 respectively. These present results show that the CF suppression factor decreases with increasing deformation of the target nuclei. This means that the CF suppression factor is not unique for the systems having the same projectile. Therefore, the effect of target deformation is clearly observed in the suppression of EFFs. Further, the total fusion functions (TFFs) for these systems were calculated by considering the total fusion cross sections (sum of CF and ICF cross sections). The TFFs were plotted as a function of x and are shown in Fig. 10. From this figure, it can be seen that the TFFs for all the systems are in good agreement with the UFF. This indicates that the ICF process also has a significant contribution along with CF in these measurements. In addition, to observe the nature of EFFs with deformation length ($\beta_2^T R^T$), the average values of EFFs and TFFs were estimated using the formulation for simple mathematical average for the above mentioned systems. The average values of EFFs (for CF only) and TFFs (for CF and ICF) were plotted as a function of $\beta_2^T R^T$ and are shown in Fig. 11. In the figure, $\langle U(x)_{\rm CF}\rangle$ and $\langle U(x)_{\rm CF+ICF}\rangle$ represent the average values of EFFs and TFFs respectively. These figures show that the average values of both EFFs and TFFs are decreasing with deformation parameter $\beta_2^T R^T$. The dash-dotted line represents the average value of the UFF in the present energy regime. In Fig. 11(a) for the system ^{16}O + ^{124}Sn, the average value of the EFF matches the average value of the UFF, while it is suppressed for other systems. The target ^{124}Sn is spherical and therefore no effect of deformation was observed. From Fig. 11(b), it can be seen that the average value of the TFF shifts towards the line corresponding to average value of the UFF for all systems with deformed targets. The average value of the TFF for the system ^{16}O + ^{124}Sn was found to be larger than the average value of the UFF. In these figures, the effect of target deformation is clearly seen in the reduction process of the UFF. These results indicate that the effect of target deformation along with the contribution of ICF must be included in the calculations of total fusion cross sections. Hence, the present study shows that the deformation of the target also strongly affects the ICF dynamics.

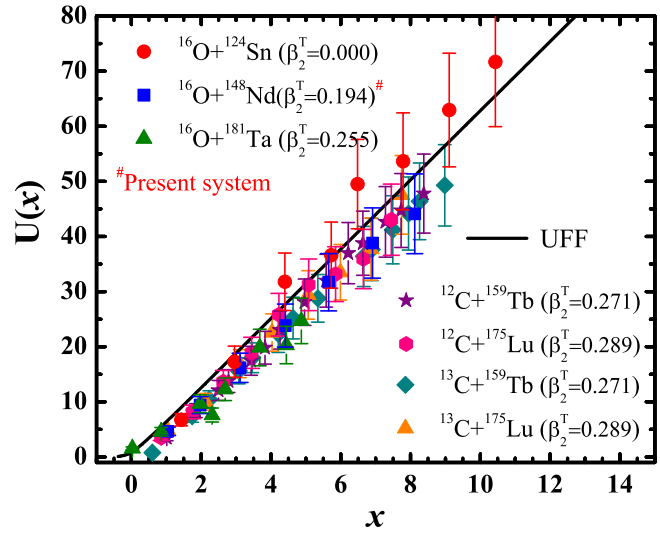

FIG. 10. The total fusion functions (TFFs) along with the universal fusion function (UFF) for the ^{16}O + ^{148}Nd system with some other systems from literature [40–43,54]. The solid line represents the UFF.

VI. SUMMARY AND CONCLUSIONS

The EFs of ERs populated via CF and/or ICF dynamics in the ^{16}O + ^{148}Nd system were measured at projectile

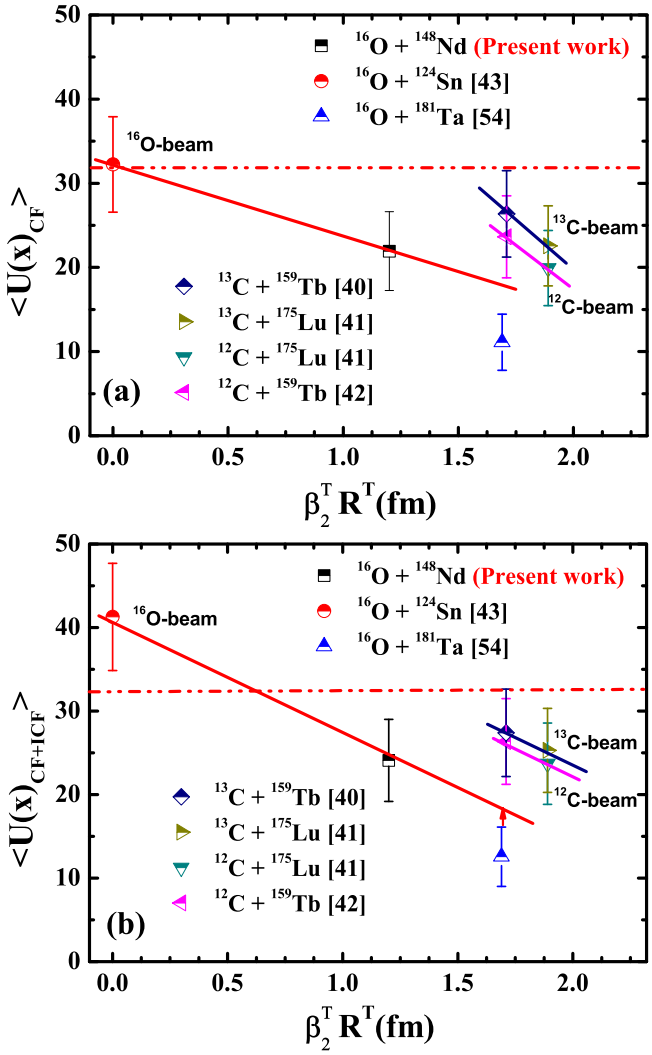

FIG. 11. (a) The average experimental fusion function (EFF) and (b) average total fusion function (TFF) as a function of deformation parameter ($\beta_2^T R^T$) of the target for the $^{16}\mathrm{O} + ^{148}\mathrm{Nd}$ system with some other systems from literature [40–43,54]. The dotted line corresponds to the mean value of UFF in this energy range. The solid lines just guide the eyes to represent the same projectiles.

energies ≈4–7 MeV/nucleon. The measured cross sections were compared with theoretical cross sections of statistical model code PACE-4. Significant enhancement was observed in measured cross sections over their theoretical predictions in α-emitting channels. These enhancements show that the ERs ^{157}Dy($\alpha 3n$), ^{155}Dy($\alpha 5n$), and ^{155}Tb($\alpha p4n$) are found to be produced through the breakup of projectile ^{16}O into $^{12}\mathrm{C} + \alpha$ (ICF process) along with the CF process. A comparison of the measured total transfer yields of ICF (α-emitting) channels with their theoretical yields using the sum-rule model suggests that the sum-rule model is not able to predict successfully the cross sections of ICF channels at low projectile energy. These results show that the sum-rule model in its present form is not valid at low projectile energies ≈4–7 MeV/nucleon. A comprehensive study was done to understand the dependence of ICF dynamics on existing entrance channel parameters, namely, mass asymmetry, Coulomb factor ($Z_P Z_T$), and α-Q value of the projectile. The present work shows that the ICF probability increases exponentially with these parameters. Further, the dependence of ICF dynamics on target deformation using deformation parameter (β_2^T) and two new parameters, deformation length ($\beta_2^T R^T$) and neutron excess $(N-Z)^T$ of the target, was studied. It was noticed that the ICF fraction rises exponentially with β_2^T, $\beta_2^T R^T$, and $(N-Z)^T$. These present results clearly indicate that the ICF fraction follows an exponential pattern rather than a simple linear growth with entrance channel parameters as suggested by earlier works. This study reveals that the ICF dynamics is strongly affected by the structure of both projectile as well as target.

Efforts were also made to confirm these effects using the universal fusion function (UFF). The experimental fusion functions (EFFs) for the system $^{16}\mathrm{O} + ^{148}\mathrm{Nd}$ along with some other systems were found to be well suppressed compared to the UFF. These present results reveal that the CF suppression factor decreases with increasing deformation of target nuclei. Moreover, the total fusion functions (TFFs) for all the systems are found to be in good agreement with the UFF. Further, to observe the nature of fusion functions with deformation parameters, the averages of EFFs and TFFs were estimated and plotted as a function of $\beta_2^T R^T$. The average values of EFFs and TFFs were found to decrease with $\beta_2^T R^T$. It was also observed that the average value of EFFs for the system $^{16}\mathrm{O} + ^{124}\mathrm{Sn}$ with a spherical target coincides with the average value of the UFF, but it is suppressed for other systems having deformed targets. The average value of TFFs for all systems with deformed targets shifts towards the average value of the UFF. In conclusion, the effect of target deformation was clearly observed along with ICF in the reduction process of the UFF. This study shows that the effect of target deformation plays an important role to affect the ICF dynamics along with various entrance channel parameters of the system.

ACKNOWLEDGMENTS

The authors are thankful to the Director and Convener, AUC, Inter-University Accelerator Centre (IUAC), New Delhi, India, for providing the necessary experimental facilities to carry out the experiments. The authors are thankful to the Target Laboratory In-Charge, Mr. Abhilash S. R., and the operational staff of the Pelletron Accelerator, IUAC, New Delhi, for providing good cooperation during the course of this experiment. D.S. acknowledges encouragement from the Vice-Chancellor of the Central University of Jharkhand (CUJ), Ranchi, India. The authors express their thanks to the Head, Department of Physics, CUJ, Ranchi, for their motivation and support. One of the authors, P.K.G. thanks IUAC New Delhi for providing financial assistance in the form of a project fellowship (Ref. IUAC/XIII.3/UFR/54321) under Dr. Dharmendra Singh. The authors are also thankful to Dr. R. Tripathi, BARC, for scientific discussions.

[1] D. J. Parker, J. J. Hogan, and J. Asher, Phys. Rev. C **35**, 161 (1987).
[2] P. Vergani, E. Gadioli, E. Vaciago, E. Fabrici, E. Gadioli Erba, M. Galmarini, G. Ciavola, and C. Marchetta, Phys. Rev. C **48**, 1815 (1993).
[3] M. Crippa, E. Gadioli, P. Vergani, G. Ciavola, C. Marchetta, and M. Bonardi, Z. Phys. A **350**, 121 (1994).
[4] D. Singh, M. Afzal Ansari, R. Ali, N. P. M. Sathik, and M. Ismail, J. Phys. Soc. Jpn. **75**, 104201 (2006).
[5] H. C. Britt and A. R. Quinton, Phys. Rev. **124**, 877 (1961).
[6] T. Inamura, M. Ishihara, T. Fukuda, T. Shimoda, and H. Hiruta, Phys. Lett. B **68**, 51 (1977)
[7] C. Gerschel, Nucl. Phys. A **387**, 297 (1982).
[8] B. S. Tomar, A. Goswami, A. V. R. Reddy, S. K. Das, P. P. Burte, S. B. Manohar, and B. John, Phys. Rev. C **49**, 941 (1994); B. S. Tomar, A. Goswami, G. K. Gubbi, A. V. R. Reddy, S. B. Manohar, B. John, and S. K. Kataria, *ibid.* **58**, 3478 (1998).
[9] D. Singh, M. A. Ansari, R. Ali, N. P. M. Sathik, B. S. Tomar, and M. Ismail, J. Phys. Soc. Jpn. **82**, 114201 (2013).
[10] D. Singh, R. Ali, M. A. Ansari, B. S. Tomar, M. H. Rashid, R. Guin, S. K. Das, R. Kumar, R. P. Singh, S. Muralithar, and R. K. Bhowmik, Pramana J. Phys. **82**, 683 (2014).
[11] H. Morgenstern, W. Bohen, W. Galster, K. Grabisch, and A. Kyanowski, Phys. Rev. Lett. **52**, 1104 (1984).
[12] M. Shuaib, V. R. Sharma, A. Yadav, P. P. Singh, M. K. Sharma, D. P. Singh, R. Kumar, R. P. Singh, S. Muralithar, B. P. Singh, and R. Prasad, Phys. Rev. C **94**, 014613 (2016).
[13] H. Kumar, S. A. Tali 1, M. Afzal Ansari, D. Singh, R. Ali, K. Kumar, N. P. M. Sathik, A. Ali, S. Parashari, R. Dubey, I. Bala, R. Kumar, R. P. Singh, and S. Muralithar, Eur. Phys. J. A **54**, 47 (2018).
[14] D. Singh, P. K. Giri, A. Mahato, S. B. Linda, H. Kumar, M. A. Ansari, R. Ali, S. A. Tali, M. H. Rashid, R. Guin, and S. K. Das, Nucl. Phys. A **981**, 75 (2019).
[15] D. Singh, P. K. Giri, A. Mahato, S. B. Linda, R. Tripathi, Harish Kumar, M. Afzal Ansari, N. P. M. Sathik, R. Ali, R. Kumar, S. Muralithar, and R. P. Singh, Phys. Lett. B **774**, 7 (2017).
[16] T. Udagawa and T. Tamura, Phys. Rev. Lett. **45**, 1311 (1980); Phys. Lett. B **116**, 311 (1982).
[17] J. Wilczynski, K. Siwek-Wilczynaska, J. Van-Driel, S. Gonggrijp, D. C. J. M. Hageman, R. V. F. Janssens, J. Lukasiak, R. H. Siemssen, and S. Y. Van Der Werf, Nucl. Phys. A **373**, 109 (1982).
[18] J. P. Bondrof, J. N. De, G. Fai, A. O. T. Karvinen, and J. Randrup, Nucl. Phys. A **333**, 285 (1980).
[19] R. Weiner and M. Westrom, Nucl. Phys. A **286**, 282 (1977).
[20] L. F. Canto, P. R. S. Gomes, J. Lubian, L. C. Chamon, and E. Crema, J. Phys. G: Nucl. Part. Phys. **36**, 015109 (2009).
[21] L. F. Canto, P. R. S. Gomes, J. Lubian, L. C. Chamon, and E. Crema, Nucl. Phys. A **821**, 51 (2009).
[22] C. Y. Wong, Phys. Rev. Lett. **31**, 766 (1973).
[23] A. Gavron, Phys. Rev. C **21**, 230 (1980).
[24] M. Thakur, R. Dubey, S. R. Abhilash, B. R. Behera, B. P. Mohanty, D. Kabiraj, S. Ojha, and H. Duggal, MethodsX **3**, 542 (2016).
[25] J. F. Ziegler, M. D. Ziegler, and J. P. Biersack, Nucl. Instrum. Methods Phys. Res., Sect. B **268**, 1818 (2010).
[26] B. P. Ajith Kumar, E. T. Subramaniam, K. Singh, and R. K. Bhowmik, in DAE-BRNS Nuclear Physics Symposium, Kolkata, 2001 (unpublished), http://www.iuac.res.in/NIAS/
[27] S. Y. F. Chu, L. P. Ekstrom, and R. B. Firestone, The Lund/LBNL Nuclear Data Search, Version 2.0, 1999, http://nucleardata.nuclear.lu.se/toi/index.asp
[28] National Nuclear Data Centre, Brookhaven National Laboratory, https://www.nndc.bnl.gov/chart/chartNuc.jsp
[29] M. A. Ansari, R. K. Y. Singh, M. L. Sehgel, V. K. Mittal, D. K. Avasthi, and I. M. Govil, Ann. Nucl. Energy **11**, 607 (1984).
[30] W. Hauser and H. Feshbach, Phys. Rev. **87**, 366 (1952).
[31] R. Bass, Phys. Rev. Lett. **39**, 265 (1977).
[32] F. D. Becchetti and G. W. Greenlees, Phys. Rev. **182**, 1190 (1969).
[33] P. M. Endt, At. Data Nucl. Data Tables **26**, 47 (1981).
[34] A. H. Wapstra and G. Audi, Nucl. Phys. A **432**, 55 (1985).
[35] J. P. Lestone, Phys. Rev. C **53**, 2014 (1996).
[36] R. Broda, M. Ishihara, B. Herskind, H. Oeschler, S. Ogaza, and H. Ryde, Nucl. Phys. A **248**, 356 (1975).
[37] M. Cavinato, E. Fabrici, E. Gadioli, E. Gadioli Erba, P. Vergani, M. Crippa, G. Colombo, I. Redaelli, and M. Ripamonti, Phys. Rev. C **52**, 2577 (1995).
[38] S. A. Tali, H. Kumar, M. A. Ansari, A. Ali, D. Singh, R. Ali, P. K. Giri, S. B. Linda, S. Parashari, R. Kumar, R. P. Singh, and S. Muralithar, Nucl. Phys. A **970**, 208 (2018).
[39] V. R. Sharma, A. Yadav, P. P. Singh, D. P. Singh, S. Gupta, M. K. Sharma, I. Bala, R. Kumar, S. Murlithar, B. P. Singh, and R. Prasad, Phys. Rev. C **89**, 024608 (2014).
[40] A. Yadav, V. R. Sharma, P. P. Singh, D. P. Singh, M. K. Sharma, U. Gupta, R. Kumar, B. P. Singh, R. Prasad, and R. K. Bhowmik, Phys. Rev. C **85**, 034614 (2012).
[41] H. Kumar, S. A. Tali, M. A. Ansari, D. Singh, R. Ali, K. Kumar, N. P. M. Sathik, S. Parashari, A. Ali, R. Dubey, I. Bala, R. Kumar, R. P. Singh, and S. Muralithar, Nucl. Phys. A **960**, 53 (2017).
[42] A. Yadav, V. R. Sharma, P. P. Singh, R. Kumar, D. P. Singh, Unnati, M. K. Sharma, B. P. Singh, and R. Prasad, Phys. Rev. C **86**, 014603 (2012).
[43] D. Singh, S. B. Linda, P. K. Giri, A. Mahato, R. Tripathi, H. Kumar, S. A. Tali, S. Parashari, A. Ali, R. Dubey, M. A. Ansari, R. Kumar, S. Muralithar, and R. P. Singh, Phys. Rev. C **97**, 064610 (2018).
[44] A. Sharma, B. B. Kumar, S. Mukherjee, S. Chakrabarty, B. S. Tomar, A. Goswami, and S. B. Manohar, J. Phys. G: Nucl. Part. Phys. **25**, 2289 (1999).
[45] U. Gupta, P. P. Singh, D. P. Singh, M. K. Sharma, A. Yadav, R. Kumar, B. P. Singh, and R. Prasad, Nucl. Phys. A **811**, 77 (2008).
[46] K. Kumar, T. Ahmad, S. Ali, I. A. Rizvi, A. Agarwal, R. Kumar, K. S. Golda, and A. K. Chaubey, Phys. Rev. C **87**, 044608 (2013).
[47] K. S. Babu, R. Tripathi, K. Sudarshan, B. D. Shrivasava, A. Goswami, and B. S. Tomar, J. Phys. G: Nucl. Part. Phys. **29**, 1011 (2003).
[48] R. Ali, D. Singh, M. Afzal Ansari, M. H. Rashid, R. Guin, and S. K. Das, J. Phys. G: Nucl. Part. Phys. **37**, 115101 (2010).
[49] D. Singh, R. Ali, M. Afzal Ansari, B. S. Tomar, M. H. Rashid, R. Guin, and S. K. Das, Phys. Rev. C **83**, 054604 (2011).
[50] D. Singh, Rahbar Ali, M. A. Ansari, M. H. Rashid, R. Guin, and S. K. Das, Nucl. Phys. A **879**, 107 (2012).

[51] S. A. Tali, H. Kumar, M. A. Ansari, A. Ali, D. Singh, R. Ali, P. K. Giri, S. B. Linda, R. Kumar, S. Parashari, S. Muralithar, and R. P. Singh, Phys. Rev. C **100**, 024622 (2019).

[52] P. Moller, A. Sierk, T. Ichikawa, and H. Sagawa, At. Data Nucl. Data Tables **109-110**, 1 (2016).

[53] W. Wilcke, J. Birkelund, H. Wollersheim, A. Hoover, J. Huizenga, W. Schrder, and L. Tubbs, At. Data Nucl. Data Tables **25**, 389 (1980).

[54] D. P. Singh, Unnati, P. P. Singh, A. Yadav, M. K. Sharma, B. P. Singh, K. S. Golda, R. Kumar, A. K. Sinha, and R. Prasad, Phys. Rev. C **80**, 014601 (2009).